Available online at www.sciencedirect.com
ScienceDirect
ELSEVIER
Ultramicroscopy 107 (2007) 345–355
ultramicroscopy
www.elsevier.com/locate/ultramic

Separation of bulk and surface-losses in low-loss EELS measurements in STEM

K.A. Mkhoyan[a,*], T. Babinec[a,b], S.E. Maccagnano[a], E.J. Kirkland[a], J. Silcox[a]

[a]*School of Applied and Engineering Physics, Cornell University, Ithaca, NY 14853, USA*
[b]*Physics Department, University of Michigan, Ann Arbor, MI 48109, USA*

Received 24 May 2006; received in revised form 2 September 2006; accepted 20 September 2006

Abstract

To identify major features in low electron energy loss spectra, the different excitations (bulk plasmons, interband transitions, surface plasmons, Cherenkov and surface guided modes) must be delineated from each other. In this paper, this process is achieved by noting the linear thickness dependence of bulk processes contrasted with the constant thickness behavior of surface excitations. An alternative approach of analyzing bulk plasmon-loss is also introduced. Using a new algorithm, the parameters of plasma generation—plasmon energy $E_{P,0}$, a damping parameter ΔE_P and the coefficient of the dispersion relation γ were obtained from a single curve fitting on the example of Si. The ability to separate surface-losses from the rest of the data permitted identification of the fine structure of the surface-losses. The strong peak at 8.2 eV characteristic of non-radiative surface plasmon excitations was measured for Si. Analysis of surface excitations indicates that a 10 Å SiO_2 surface coating layer is still present despite careful cleaning the specimen. Dielectric functions deduced from the EELS data prove to be considerably affected by the presence of the surface-losses for samples as thick as 800 Å.

PACS: 73.20.Mf; 77.22.Ch; 61.16.Bg

Keywords: EELS; STEM; Bulk plasmon-loss; Surface-loss; Dielectric function; Si

1. Introduction

The value of analytical scanning transmission electron microscopy (STEM) for the characterization of materials is based primarily on its ability to carry out measurements on a scale as small as its probe size, which now can reach 0.8 Å [1]. A STEM equipped with a *Z*-contrast annular dark field (ADF) detector and an electron-energy-loss spectrometer (EELS) provides the capability to identify not only individual dopant atoms [2] but also to measure changes in local (atomic scale) electronic structures induced by dislocations [3,4] or by a single dopant atom [5]. Unfiltered EELS with energy resolution of ~0.5 eV flattens sharp features of spectra to the point of invisibility. The emerging capability of improved energy resolution, for example down to 200 meV or better, raises the interesting possibility of increasing the visibility of such sharp features (e.g., in electronic transitions) in the low energy loss region. Better analysis than has been carried out so far will be necessary to achieve quantitative analysis of spectra. In particular, the collective components of the spectrum (e.g., bulk plasmon, surface plasmon and Cherenkov radiation losses) need careful characterization. For example, separation of the bulk and surface plasmon energy loss spectra is required in order to invert the bulk response ($Im\{-1/\varepsilon\}$) to find ε, the true dielectric response function.

The response of the specimen to a fast electron passing through is a function not only of the energy lost due to inelastic interactions, but also of the momentum transferred, $\hbar\vec{q} = \hbar\vec{k_0} - \hbar\vec{k'}$ [6–9]. In STEM, however, measured EELS spectra are angle-integrated given a convergent incident beam and finite collection aperture. Fig. 1 shows a simple ray diagram with incident momentum $\hbar\vec{k_0}$ and scattered momentum $\hbar\vec{k'}$ electrons in STEM. Sorting EELS by transferred momentum, $\hbar\vec{q}$, in the STEM is thus limited

*Corresponding author. Tel.: +1 607 255 0649; fax: +1 607 255 7658.
E-mail address: kam55@cornell.edu (K.A. Mkhoyan).

0304-3991/$ - see front matter © 2006 Elsevier B.V. All rights reserved.
doi:10.1016/j.ultramic.2006.09.003

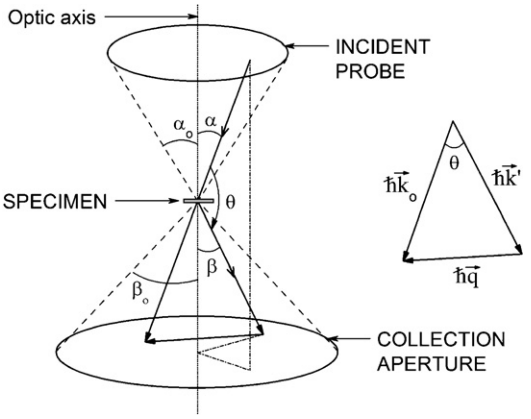

Fig. 1. Simple ray diagram of incident and scattered electrons in STEM. The incident beam convergent angle is α_0 and maximum collection angle is β_0. The angle between the incident $\vec{k_0}$ and scattered $\vec{k'}$ wave-vectors is defined by θ. Note that $\vec{k'}$ is not necessarily in the plane formed by $\vec{k_0}$ and the optic axis.

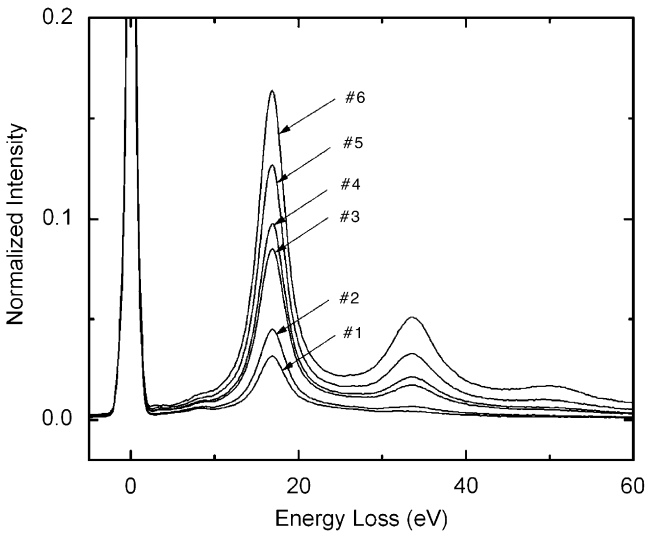

Fig. 2. Six low-loss EELS data recorded from a Si sample at different thicknesses. Spectra are scaled to have the same zero-loss peak intensity (normalized to one). The labels are from the thinnest, #1, to the thickest, #6.

by the poorer momentum resolution relative to that available in CTEM [8,10–13]. Corrections to EELS data have been made earlier for some simple geometries [14]. For the particular case of uniaxial crystals, Browning et al. [15] introduced an integration-based approach to separate the *c* and *a* components in core-level EELS.

Low-loss EELS spectra (0–70 eV) are also complicated by the mixture of both surface and bulk excitations. In this paper we separate bulk excitations from surface excitations for isotropic materials by exploiting differences in the thickness dependence. This leads to quantitative analysis of each of these losses. It is shown that the parameters of bulk plasmon excitations can be retrieved using a numerical fitting algorithm. Spectra of surface-losses allow quantification of the surface coating layer. Finally, the effects of the surface-losses in determination of the dielectric function deduced from low-loss spectra are discussed as well.

2. STEM measurements

Low-loss EELS measurements were carried out on the Cornell 100 kV VG HB-501 STEM. This microscope has a field emission gun, a high resolution pole piece with spherical and chromatic aberration coefficients of $C_s = 1.3$ mm and $C_c \simeq 1.5$ mm, and can achieve a 2 Å in diameter circular probe. It is also equipped with an ADF detector for *Z*-contrast imaging and an electron spectrometer for energy loss spectroscopy. During data acquisition the microscope was operated with a 10 mrad incident beam convergent angle and a 21.5mrad collection aperture. The energy resolution of the spectrometer is 0.7 eV with an energy drift of <0.03 eV/min over the energy range of 0–2 keV [16]. Silicon specimens were prepared by standard tripod polishing, using a commercially available Si [1 0 0] wafer. After mechanical polishing, a 4° wedge specimen was briefly dipped in 10% HF solution to remove the surface oxide. However, a thin layer of SiO_x may still be present due to exposure to air before loading into the STEM.

The specimen was tilted away from zone axes to avoid strong diffraction of the incident beam. EELS data were recorded in area mode from a 12×12 nm^2 square region to minimize electron-beam-induced damage. Six low-loss spectra were recorded at different specimen thicknesses. Since data acquisition required a considerable amount of time ($\gtrsim$30 min), some differences ($<$20%) in the incident beam current are expected between data sets [16]. Fig. 2 shows six low-loss EELS spectra normalized to the zero-loss peak to highlight the effects of the thickness on the intensities of the first, second and third plasmon-losses. Each spectrum presented here is an average of about 200 individually recorded EELS spectra to improve S/N ratio. The dark current was subtracted from all six spectra.

3. Data analysis

Normalization of the recorded spectra for further analysis can be carried out in two ways: (i) by absolute normalization, where each spectrum is normalized to a single incident electron or (ii) by relative normalization, where some peaks of the EELS data are normalized relative to others. While absolute normalization is required for direct comparison of the measured spectrum with theoretically predicted cross-sections, obtaining such normalization is difficult. Exact knowledge of the incident beam current, which may vary from one measurement to another depending on tip condition and extraction voltage, and accurate knowledge of the parameters of the electron optics and beam spreading inside the specimen are essential. To stress the importance of the beam spreading in particular, the angular distribution of the probe at different

thicknesses is calculated for an amorphous Si sample. The results of calculations based on the multislice method [17,18] are presented in Fig. 3. The simulations indicate that under typical STEM optics (10 mrad convergent beam and 21.5 mrad collection aperture) only 60% of the original beam will reach the EELS detector after passing through 1000 Å of *a*-Si, and only 30% if an 8.5 mrad collection aperture is used. The effects will be even more dramatic if a crystalline specimen oriented along a zone axis is under investigation. In this paper we limit ourselves to relative normalization to avoid most of problems described above, though the effects of beam spreading will remain. As will be seen in the following sections, many properties of the specimen can still be retrieved quantitatively using relative normalization.

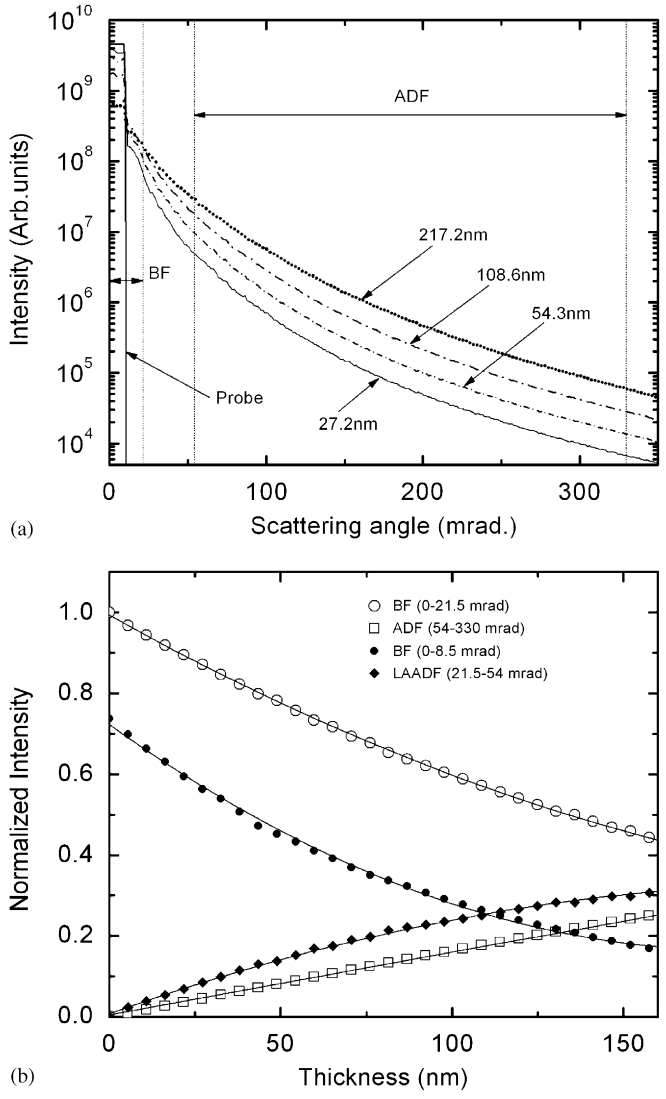

Fig. 3. Calculated electron beam spread after passing through *a*-Si of different thicknesses: (a) angular distribution of the beam; (b) fraction of the initial beam scattered into BF/EELS and ADF detectors. The inner and outer angles of each detector are indicated. A linear fit to the ADF data and parabolic fits to the BF and low-angle ADF (LAADF) data are also presented (solid lines). In these calculations the STEM probe convergence angle is 10 mrad, $C_s = 1.3$ mm and $\Delta f = 850$ Å.

For analysis of the response of the specimen to incident fast electrons, spectra with single inelastic scattering distributions (SSDs) must be obtained. For removal of multiple scattering from recorded EELS data, the Fourier-log deconvolution method [19] was implemented giving the SSD as

$$s(v) = z(v) \ln\left[\frac{j(v)}{z(v)}\right], \quad (1)$$

where $j(v)$ and $z(v)$ are the Fourier transforms of the recorded EELS data and zero-loss spectrum. It should be noted that this simple method ignores the complications due to angular convolutions in the multiple scattering [8,20,21]. However, we can argue that these effects are small in the framework of the analysis presented here and can be safely ignored since the angular effects that are due to multiple bulk plasmon-loss are significant only for energies bigger than twice the energy of the bulk plasmon ($>2E_{P,0}$). The effects due to double surface losses or single surface and single bulk plasmon losses are also small since the contribution to the EELS data from surface-losses in all measurements presented here is an order of magnitude smaller than that from bulk plasmon-losses.

The SSDs for all six thicknesses were retrieved using Eq. (1), four of which are presented in Fig. 4. In Fig. 4(b) the SSDs are scaled to the peak of the bulk plasmon-loss, thus highlighting the increasing relative contribution of surface-losses in thinner samples. With a zero-loss spectrum, $Z(E)$ (or $z(v) = FT[Z(E)]$), recorded under identical conditions as the rest of the EELS measurements but without a specimen, it should be possible in principle to not only accurately determine the band gap of the specimen but to also locate electronic states present in the gap and even peaks corresponding to phonon-losses if energy resolution permits. However, all the measurements presented here were recorded with 0.7 eV energy resolution and 0.22 eV channel size, so it is virtually impossible to quantify features located below 2 eV. As a result, the value of the band gap obtained here is inaccurate as can be seen in Fig. 4(b). A determination of the band gap in silicon using EELS analysis has been reported previously by Batson [22,23].

3.1. Separating bulk-losses and surface-losses

A critical parameter essential for the separation of bulk and surface losses is the thickness of the area from where the EELS data was recorded. Since the probability of bulk plasmon excitation obeys Poisson statistics [24] to a good approximation, the thickness of the area can be estimated by calculating the ratio of the first plasmon-loss integrated intensity to the zero-loss integrated intensity:

$$I_{PL}^{(1)}/I_0 = t/\lambda_{PL}. \quad (2)$$

The thickness, t, is determined in units of the mean-free-path, λ_{PL}. The mean-free-path has a slight dependence on the electron optical conditions of the microscope (objective

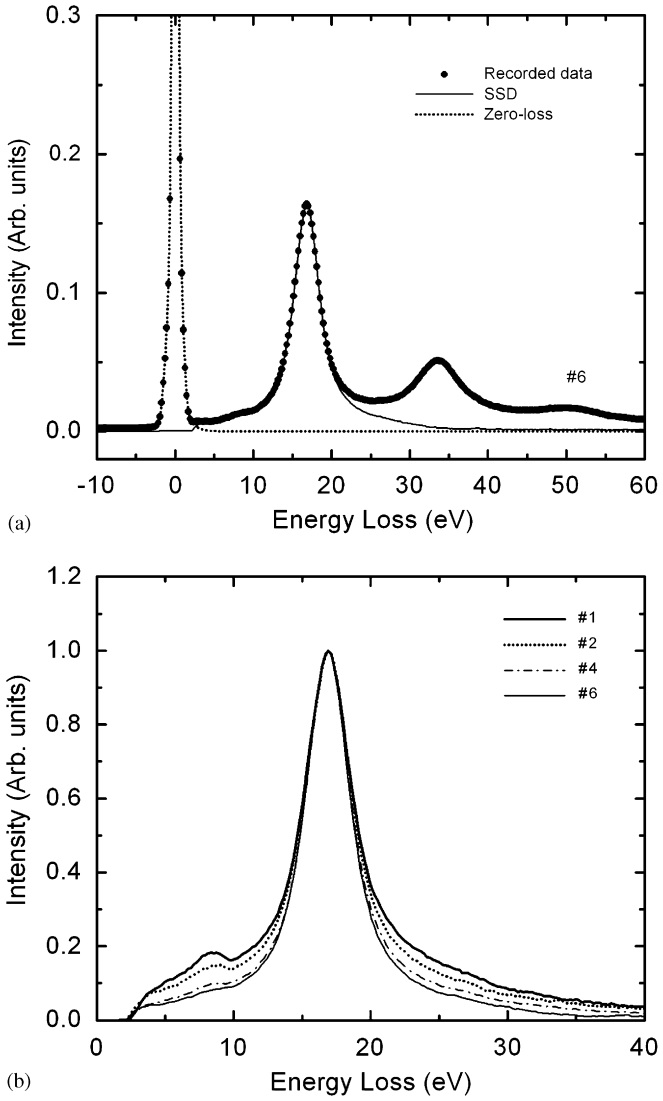

Fig. 4. (a) Low-loss spectra from the silicon sample before and after Fourier-log deconvolution: (b) the single scattering distributions obtained for four different thicknesses. The original EELS data are presented in Fig. 2. The spectra are scaled to the peak of the bulk plasmon-loss.

and collection aperture sizes) [9]. However, since the dependence is weak the value of $\lambda_{PL}(Si) = 121$ nm can be used [25] to a good approximation for the experimental conditions used here. For generalization of the results in the analysis that follows, the thicknesses of the specimens are discussed both in actual values as well as in the units of λ_{PL}.

To estimate the thickness with Eq. (2) the isolated spectrum of the bulk plasmon is needed. Since SSDs contain bulk plasmon-loss spectra as well as surface losses, the following procedure is applied: to a first approximation it is assumed that the SSD obtained from the thickest area (spectrum #6 with $t \sim 150$ nm) is dominated by the bulk plasmon-loss and the contribution of surface effects is negligible and then the ratio of the integrated intensities and peak heights of the first plasmon-loss to zero-loss are calculated. The ration of the first value to the second is defined as a correction coefficient. The thicknesses for the areas #1 to #6 are now estimated using the respective rations of the peak heights of the first plasmon and zero-loss multiplied by correction coefficient. The results are 26.0, 36.5, 69.5 79.5, 103.0 and 133.0 nm, respectively. Improved estimates of the thickness can be obtained by successive iterations:

Step 1: estimate thickness using thick area as reference (1st iteration).

Step 2: estimate the contribution of surface losses.

Step 3: remove surface losses.

Step 4: estimate thickness using new bulk plasmon loss (2nd iteration).

Step 5: go to Step 2.

The values for thicknesses after the second iteration are 32.0, 42.0, 73.5, 82.5, 103.0 and 129.0 nm and do not change significantly after further iterations.

The SSD, in general, can be expressed as a sum of bulk and surface losses:

$$I_{SSD}(E,t) = I_b(E,t) + I_s(E,t), \tag{3}$$

where each term has a different thickness dependence. The bulk loss has a simple linear thickness dependence:

$$I_b(E,t) = t \cdot [I_{PL}(E) + I_{Int}(E) + I_{Ch}(E)], \tag{4}$$

where I_{PL}, I_{Int} and I_{Ch} are the spectra of the bulk plasmon-loss, interband transitions and Cherenkov radiation for unit thickness. The I_{Int} and I_{Ch} contribution in the bulk loss, heavily dominated by the bulk plasmon-loss, are limited only to the region 0–10 eV and can be neglected for present purposes. The thickness dependence of the surface loss, dominated by the surface plasmon-loss, is only critical for extremely thin (<10 nm) specimens [24]. At these small thicknesses, the two surface plasmons excited at each surface of the specimen interact with each other and, as a result, the surface plasmon dispersion curve splits into two with a degree of splitting depending on the thickness of the specimen. In addition, at the limit $t \to 0$, the intensity of the surface plasmon naturally approaches 0. For the thicknesses considered here ($t > 25$ nm) $qt \gg 1$, which suggests that no significant interaction of surface plasmons should be expected [24]. The intensity of the surface loss, therefore, can be considered independent of the thickness

$$I_s(E) = I_{SP}^{top}(E) + I_{SP}^{bott}(E), \tag{5}$$

where I_{SP}^{top} and I_{SP}^{bott} are the intensities of the surface plasmons generated at the top and bottom surfaces of the specimen in the limit as $t \to \infty$.

Since surface losses are thickness independent under the specified conditions, it is intuitive to use these surface features of SSDs for normalization. However, substantial background from the tails of the bulk plasmon loss are present in the region of surface losses (0–14 eV). On the other hand, in the region around $E_{P,0}$, for thicknesses considered here, SSD is dominated by bulk plasmon-loss, and, therefore, the peak of the bulk plasmon loss can be used for normalization (see Fig. 4(b)). Eq. (3) normalized

to the bulk plasmon loss is equivalent to

$$I^{\text{new}}_{\text{SSD}}(E,t) = I_{\text{PL}}(E) + \frac{1}{t} I_{\text{s}}(E). \tag{6}$$

Expression (6) now allows us to use any two SSDs at different thicknesses to deduce surface-losses:

$$I_{\text{s}}(E) = \left(\frac{t_i \cdot t_j}{t_j - t_i}\right)[I^{\text{new}}_{\text{SSD}}(E,t_i) - I^{\text{new}}_{\text{SSD}}(E,t_j)]. \tag{7}$$

Four spectra of $I_{\text{s}}(E)$ obtained from four different pairs of SSDs are presented in Fig. 5(a). Good correlation between different surface-loss features are observed. By subtracting $I_{\text{s}}(E)$ from the SSDs using the same Eq. (6), the spectrum of the bulk plasmon loss can be obtained. Such spectra of the bulk loss for four thicknesses are presented in Fig. 5(b).

To check the accuracy of the separation procedure, the ratios of the bulk plasmon-losses to surface-losses are calculated and presented in Fig. 6(a). As expected, a linear dependence $f(t) = ct$ is observed with a coefficient of proportionality $c = 0.25$. The integrated intensities of surface losses in the SSDs were about 11% in #1 and only 3% in #6. The fraction of the first plasmon losses in the total EELS spectra were also calculated. The results presented in Fig. 6(b) show good agreement with the expected Poisson statistics.

3.2. Bulk-loss

The dispersion relation $E_{\text{P}} = \hbar\omega(q)$ of the bulk plasmon for small wave-vectors q is given as [24,26]

$$E_{\text{P}} = E_{\text{P},0} + \gamma \frac{\hbar^2}{m} q^2, \tag{8}$$

where $E_{\text{P},0}$ is the plasmon energy at $q = 0$. The coefficient γ, which the Lindhard model predicts to be $3E_{\text{F}}/5E_{\text{P},0}$, can be measured experimentally. Measured values are often different from theoretical predictions. For Si, the entire dispersion relation has been tested experimentally and

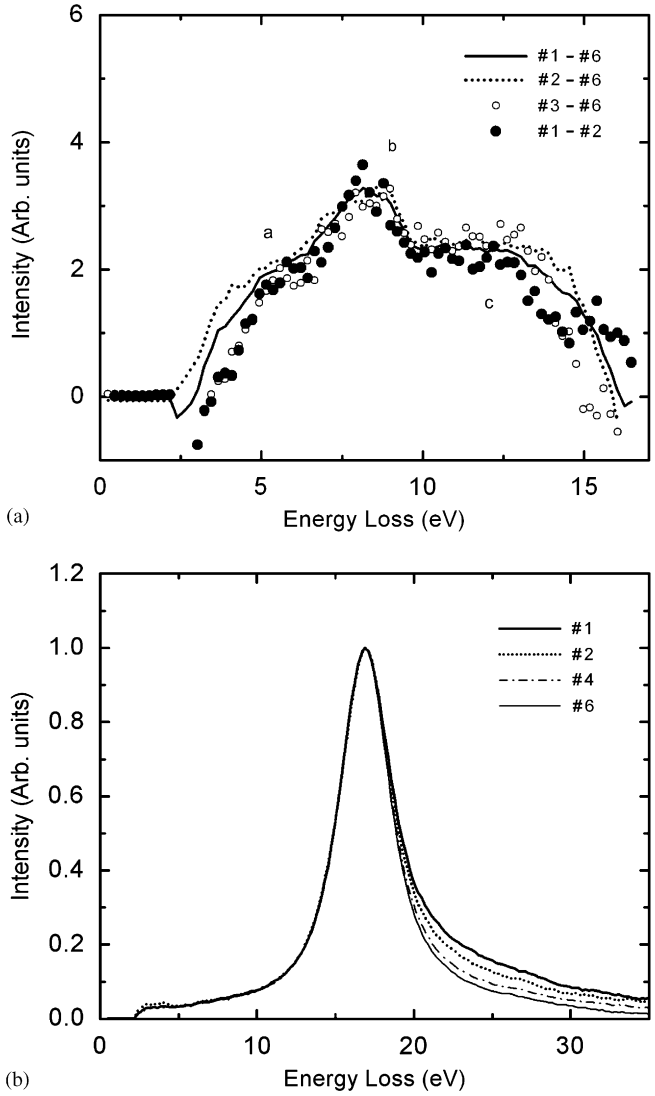

Fig. 5. (a) Surface-loss spectra of silicon obtained from several pairs of normalized SSDs with different thicknesses. For details see text. Three major features are labeled as a–c: (b) spectra of bulk-losses after removing surface-losses from SSDs (see Fig. 4(b)).

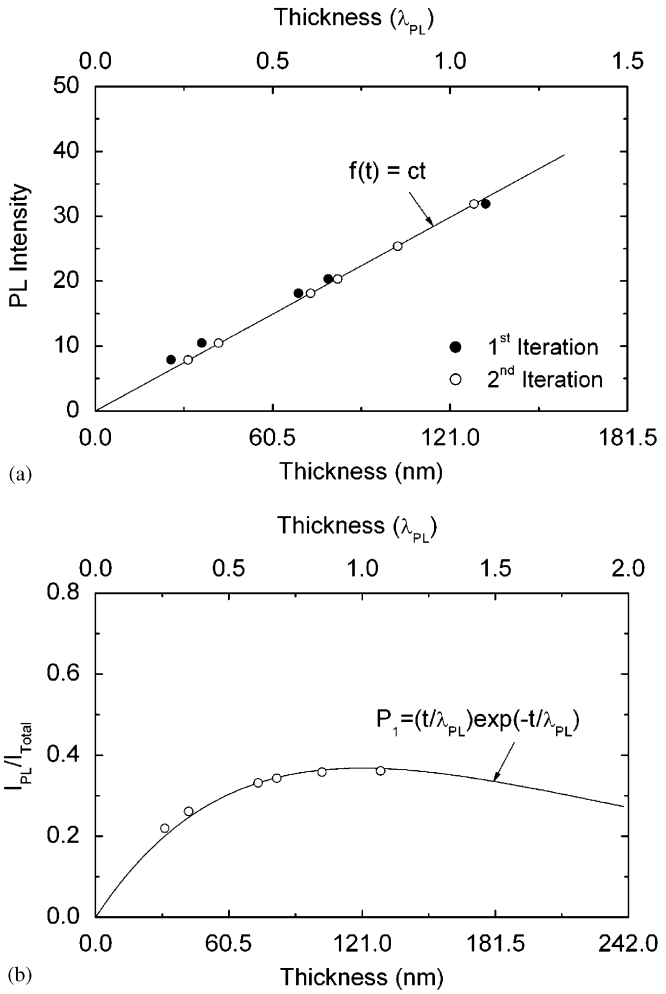

Fig. 6. (a) The ratio of the bulk-loss (plasmon-loss) to surface-loss intensities after 1st and 2nd iterations. The coefficient of the linear fit is $c = 0.25$: (b) the ratio of bulk-loss to total low-loss intensities. The value of $\lambda_{\text{PL}} = 121$ nm for plasmon-loss mean free path was used here.

values for the coefficients γ, $E_{P,0}$ have been reported [24]. These measurements were performed on conventional TEMs with angular-resolved EELS capabilities. Here we determine the coefficient γ as well as $E_{P,0}$ and the damping coefficient ΔE_P from a single STEM–EELS measurement.

The cross-section of a bulk plasmon generation by fast incident electrons, is expressed as [7,27]

$$\frac{\partial^2\sigma_b}{\partial E\,\partial\Omega} = \frac{1}{2\pi^2 n a_0}\frac{1}{E_0}\frac{1}{\theta^2+\theta_E^2} \times\left[\frac{E\Delta E_P E_{P,0}^2}{(E^2-E_{P,0}^2-\gamma 4E_{P,0}E_0(\theta^2+\theta_E^2))^2+E^2\Delta E_P^2}\right], \quad (9)$$

where n is the atomic density of specimen, a_0 is Bohr radius, E_0 is the incident electron energy. In this expression for cross-section transition from the scattering vector $\vec{q}$ to a scattering angle $\vec{\theta}$ has been made by using the relationship $q^2 = k_0^2[\theta^2+\theta_E^2]$ and introducing a characteristic angle with relativistic correction as $\theta_E = (E/E_0)[(E_0+m_0c^2)/(E_0+2m_0c^2)]$. The contour-plot of the cross-section calculated using expression (9) and presented in Fig. 7, shows a characteristic dependence on scattering angle and energy-loss. A significant drop of the cross-section with increasing scattering angle can be observed.

By integrating expression (9) over all allowed incident and collection angles [14] (for notation see Fig. 1) the energy-loss dependent cross-section corresponding to the bulk plasmon-loss spectrum can be obtained

$$\frac{\partial\sigma_b}{\partial E} = \frac{1}{\pi\alpha_0^2}\int_0^{\alpha_0}\vec{\alpha}\,d\vec{\alpha}\int_0^{\beta_0}\vec{\beta}d\vec{\beta}\frac{\partial^2\sigma_b}{\partial E\,\partial\Omega}, \quad (10)$$

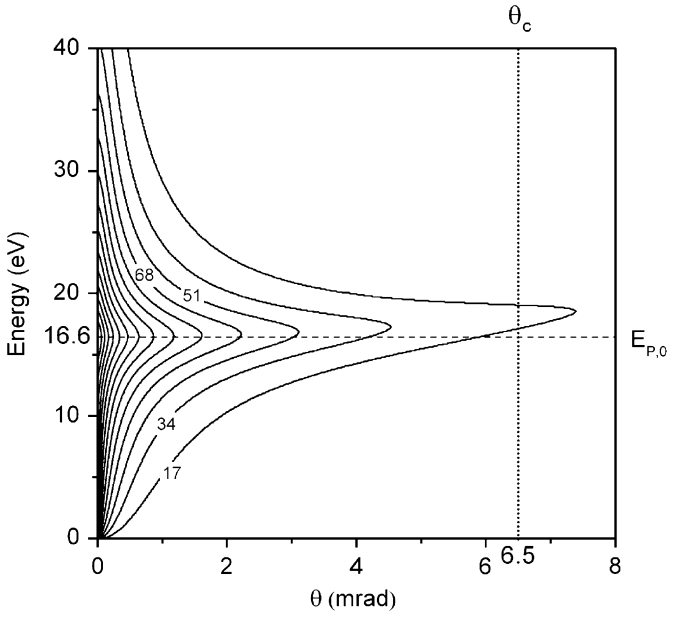

Fig. 7. Calculated cross-section of bulk plasmon excitation in a typical Si sample when excited by 100 keV electrons. The graph is on a logarithmic scale. The following values were used in simulations: $E_{P,0} = 16.6$ eV, $\Delta E_P = 3.5$ eV and $\gamma = 0.4$. The characteristic cut-off angle θ_c for Si is also indicated.

where the scattering angle is $\vec{\theta} = \vec{\alpha} - \vec{\beta}$. This function now can be fitted to experimentally measured bulk plasmon-loss spectra using γ, $E_{P,0}$ and ΔE_P as fitting parameters. To do this, first, energy-loss functions are generated by numerical integration of Eq. (10) using a multidimensional integration routine based on *Gaussian Quadrature* [28]. Then, a multidimensional *Simplex* routine [28,29] was applied to perform a least square fit. A 7–27 eV energy range was selected for that purpose. The results of fitting to bulk plasmon-losses #1 and #2 are presented in Fig. 8. The values obtained are summarized in Table 1. Good agreement with previously measured parameters is observed. The peak position of the bulk plasmon-loss in our measurements was at 16.8 ± 0.2 eV. The advantage of this approach, which is based on multidimensional fitting, is that it allows all three parameters to be obtained simultaneously.

Careful analysis shows that there is an optimal but rather wide range of thicknesses where this approach works reliably and with reasonable accuracy. For thin samples, <300 Å (or $<0.25\lambda_{PL}$), several surface-induced effects start

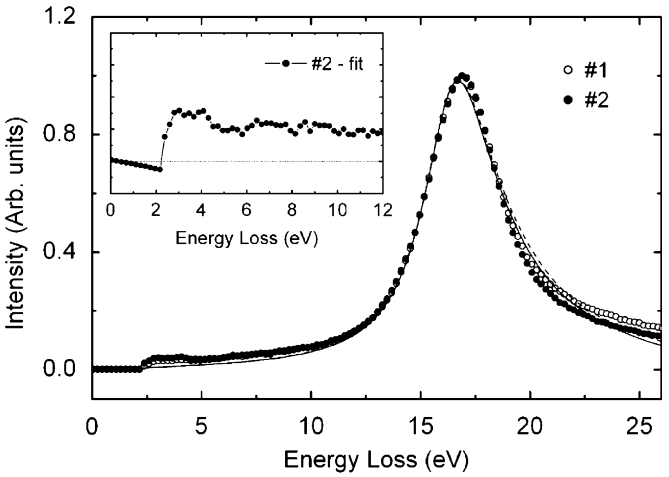

Fig. 8. Bulk-loss spectra in Si at thicknesses 320 and 420 Å dominated by the plasmon-loss, with their fits. Dash line is fit to curve #1 and the solid line to curve #2. The inset shows the difference between spectrum #2 and its fit revealing small contributions from interband transitions and Cherenkov radiation.

Table 1
The values of the parameters γ, $E_{P,0}$ and ΔE_P characterizing the bulk plasmon-loss

	Parameters		
	$E_{P,0}$ (eV)	ΔE_P (eV)	γ
This work	16.2 ± 0.2	3.3–3.4	≈ 0.2
Other works[a]	16.45 ± 0.1	3.6	
	16.5 ± 0.1	3.7 ± 0.2	
	16.9 ± 0.1	3.2 ± 0.2	
			0.32–0.41
Ref. [12]	16.6		

[a]See Ref. [24] and references in it.

to contribute: radiative surface plasmons [10] located just above $E_{P,0}$, coupling of surface plasmons [11] excited at the two surfaces, coupling of surface and bulk plasmon excitation [12], and errors in the energy region $E_{P,0}$ to $2E_{P,0}$ due to angular effects ignored in the Fourier-log deconvolution process.

For thick samples, >800 Å (or $>0.75\lambda_{PL}$), where the surface effects are now minimal, beam spreading becomes a factor (see Fig. 3). With increased thickness more electrons suffer an inelastic collision with a bigger scattering angle θ during beam propagation through a specimen. Relatively more electrons scatter outside the finite collection aperture. The result is a suppression of plasmon dispersion that induces non-uniformity of the energy-loss spectrum. It is even more pronounced when smaller collection apertures are used [30]. As the specimen thickness increases, the combination of beam spreading with plasmon excitation results in more electrons suffering an inelastic collision with a larger total scattering angle θ. Thus, relatively more electrons scatter outside the finite collection aperture. The result is an apparent suppression of the plasmon dispersion, giving non-uniformity of the energy loss spectrum. To show the scale of the effect, the fraction of electrons that suffer both a single plasmon loss coupled with an elastic collision and also scatter outside the EELS detector (about 21 mrads) is calculated and presented in Fig. 9(a) for 32 and 83 nm thick *a*-Si samples. Only the elastic and single plasmon scattering are considered and the results are plotted as a function of plasmon scattering angle.

For quantitative comparison the fraction of these electrons that were scattered outside of EELS detector while propagating from the depth of 32–83 nm were calculated. Beam propagation through the specimen and changes in intensity distributions due to elastic scattering were computed by the multislice method [18] and plasmon loss scatterings were then incorporated. The result, now as a function of energy loss, after multiplication by the cross-sections (9) was plotted in Fig. 9(b) and compared with measurements: the difference between the plasmon loss curves #1 and #4 in Fig. 5(b). An excellent match confirms that the differences in right-hand sides of plasmon loss curves in Fig. 5(b) are indeed from non-uniform scattering of electrons outside of the EELS detector.

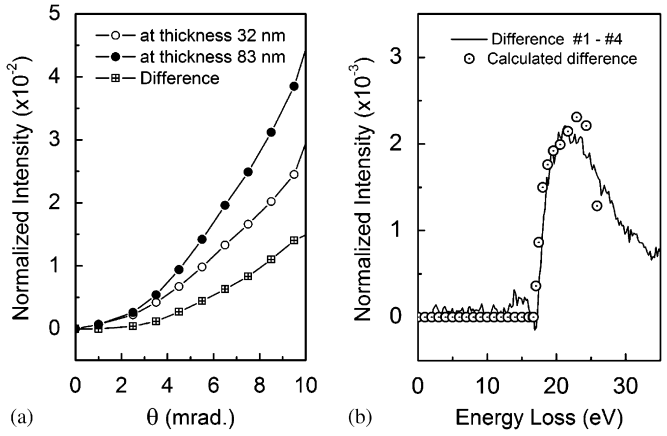

Fig. 9. (a) Intensities of the probe electrons that suffer both elastic scattering and a single plasmon loss and are scattered outside 21 mrad EELS detector as a function of plasmon-loss scattering angle. Two thicknesses of an *a*-Si specimen were considered. The elastic scattering was computed by the multislice method; (b) calculated intensity of the probe electrons that suffer plasmon loss and are scattered outside EELS detector in 32–83 nm thickness range. For comparison the corresponding difference between curves #1 and #4 in Fig. 5(b) are presented. All intensities in (a) and (b) are normalized to the total plasmon loss intensity.

The optimal thickness range for the analysis, therefore, is 300–800 Å (or 0.25–0.75 λ_{PL}). In Fig. 8 the fit to the plasmon-loss for a specimen with thickness of 420 Å (spectrum #2) is slightly better than that of 320 Å (spectrum #1). Spectrum #1 is a borderline thickness for which the method is applicable.

3.3. Surface-loss

The surface-losses presented in Fig. 5(a) consist of a well-defined peak at about 8.2 eV (peak b) with two strong shoulders on either side (a and c). The dominating feature in the spectrum is of the non-radiative surface plasmon [31–33] peak at 8.2 eV. In Si, these excitations have been studied previously by Chen et al. [12]. The region of 2–4 eV also contains excitations of guided surface waves [12,34], which are the origin of the shoulder 'a'. A considerable signal in 10–15 eV region, 'c', was also observed earlier [12] and is partially due to the presence of a surface oxide layer and partially due to the excitation of radiative surface modes [10,32]. However, a better understanding of the origins of the intensities here is needed.

Unlike bulk plasmons, the excitations of non-radiative surface plasmons are also a function of the angle between the incident electron velocity and the specimen surface normal. Therefore, specimen tilt should be taken into account in the further analysis. The non-radiative losses consist of electrons causing s- and p-polarized excitations, although the s-polarized excitations are significantly suppressed [31,33]. In the general case, when the surface normal is tilted by α_t relative to the incident electron and p-polarized excitations are considered, and the cross-section of these surface plasmon-losses is given as [31]

$$\frac{\partial^2\sigma_s}{\partial E\,\partial\Omega}=\frac{2e^2P_0^2}{\pi^2\hbar^4v^2\cos(\alpha_t)}Im\left\{\frac{(\varepsilon-\varepsilon_0)^2}{\varepsilon\varepsilon_0 L}\frac{q_s^2\Phi_1^4}{\Phi_0^4\Phi^4}\right\}, \tag{11}$$

where P_0 and v are incident electrons momentum and velocity, ε and ε_0 are dielectric functions of the specimen and the covering media ($\varepsilon_0=1$, if surfaces are clean). The function L, describe in details in Appendix A, defines dispersion relation for surface plasmons. For definitions of Φ, Φ_0 and Φ_1 see also Appendix A. The cross-section (11) has a strong dependence on q_s, the surface parallel component of the scattering vector. The cross-section (11) drops $\propto\theta^{-3}$ with scattering angle and as a result contributes significantly only at small angles ($\lesssim 0.5$ mrad). Within this small angle region the dispersion of the bulk

plasmon can be ignored and, therefore, the dielectric function of the specimen in expression (11) has a simple form

$$\varepsilon(E) = 1 - \frac{E_{P,0}^2}{E^2 + iE\Delta E_P}. \quad (12)$$

As mentioned previously a slight oxidation of the surfaces of the specimen is expected. To incorporate effects in the cross-section due to the presence of small oxide layers, the modified dispersion equation for surface plasmons must be used. The expression for L in Eq. (11) at the interface between a semi-infinite slab and superimposed layer (oxide layer) with thickness d and dielectric constant ε_0 is given by [12,35]

$$L = \chi_0\varepsilon + \chi\varepsilon_0 \frac{1 - \eta\ \exp(-2\chi_0 d)}{1 + \eta\ \exp(-2\chi_0 d)}, \quad (13)$$

where

$$\eta = \frac{\varepsilon\chi_2 - \chi_0}{\varepsilon\chi_2 + \chi_0}, \quad \chi_2 = (q_s^2 - \omega^2/c^2)^{1/2}, \quad (14)$$

and χ_0 and χ are defined in Appendix A. We do not directly compare the cross-section (11) with surface-loss measurements, since radiative losses are not included in our calculations. However, this cross-section can provide quantitative information about the surface oxide, SiO_x ($0 \leqslant x \leqslant 2$). The position of the peak in the surface-loss spectrum (8.2 eV in these measurements) has a strong dependence on the thickness of the oxide layer and the oxidation level x through the dielectric constant ε_0.

The cross-section for non-radiative surface plasmon excitation (11) is best described by tracing lines of maximum intensities showing the angular and energy dependence. In Figs. 10(a,b) the lines of maximum value are shown for different oxide thicknesses and oxidation levels. The calculations were carried out for $\alpha_t = 10^\circ$ and were averaged over azimuthal angle ϕ (see Appendix A). A slight angular asymmetry of the lines is due to non-normal incidence of the probe electrons. The angle-integrated cross-section varies slowly with tilt angle α_t and, therefore, the effects of $\pm 2^\circ$ due to the wedge shape of the specimen as well as a small angular distribution of the convergent probe ($\leqslant 10$ mrad) can be ignored. As can be seen, thicker oxide layers and lower oxidation levels move the peak to lower energies. Calculations indicate that the 8.2 eV peak observed in the measurements corresponds to the presence of fully oxidized SiO_2 that has 10 ± 2 Å thick layers on each surface of the Si sample (the dielectric constant [36] for SiO_2 is 3.9).

3.4. Dielectric function

Since EELS from the low-loss region contains quantitative information about both the real and imaginary parts of the complex dielectric function of the material, the effects of the surface losses on determination of these properties are studied here. The intensity of the single inelastic scattering obtained from low-loss EELS is proportional to the imaginary part of the complex $\{-1/\varepsilon\}$ [9,37]

$$I_{SSD}(E) \propto t \cdot Im\{-1/\varepsilon\}. \quad (15)$$

The proportionality coefficient, in general, is a function of the incident electron energy, the probe intensity and the geometry of the electron optics. Expression (15) holds only in the absence of surface excitations and, therefore, surface losses must be removed from SSD before applying it.

For derivation of the real and imaginary parts of the dielectric function, $\varepsilon = \varepsilon_1 + i\varepsilon_2$, the Kramers–Kronig dispersion relation can be used to obtain $Re\{1/\varepsilon\}$ from $Im\{1/\varepsilon\}$ [37]. A Fourier series method [38] is an efficient computational routine for this analysis. Following this, the real and imaginary parts of the dielectric function can be deduced using the following relations:

$$\varepsilon_1(E) = \frac{Re\{1/\varepsilon(E)\}}{[Re\{1/\varepsilon(E)\}]^2 + [Im\{1/\varepsilon(E)\}]^2}, \quad (16)$$

$$\varepsilon_2(E) = \frac{-Im\{1/\varepsilon(E)\}}{[Re\{1/\varepsilon(E)\}]^2 + [Im\{1/\varepsilon(E)\}]^2}. \quad (17)$$

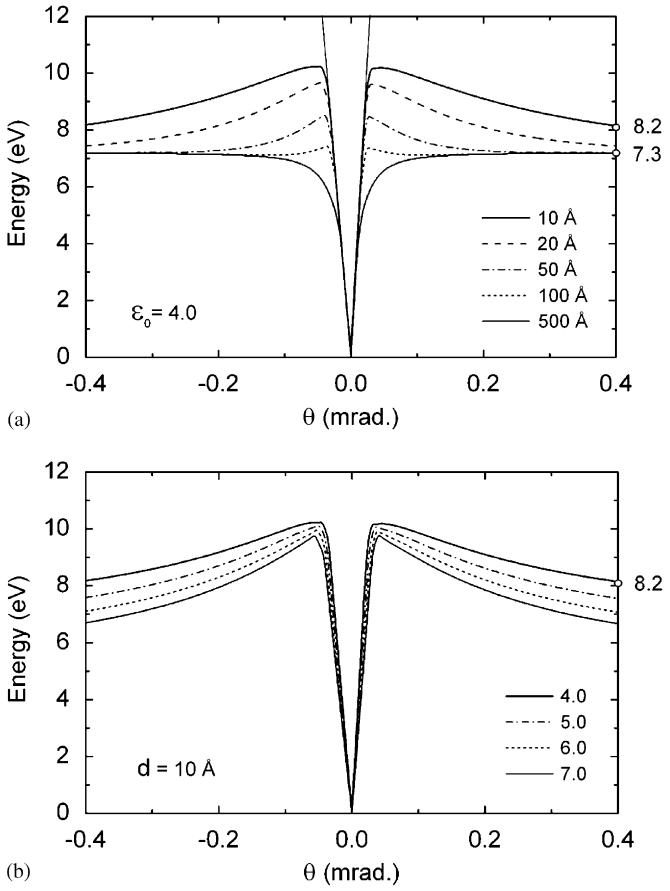

Fig. 10. The lines of maximum intensity of the cross-section for non-radiative surface plasmon-loss calculated using Eq. (11): (a) for different oxide thicknesses at $\varepsilon_0 = 4.0$ and (b) for different values of dielectric constant ε_0 for a 10 Å oxide layer. In these calculations $E_{P,0} = 16.5$ eV and $\Delta E_P = 3.4$ eV. The light lines are also graphed (nearly vertical thin lines in (a)). The peak position, 8.2 eV, and the limiting value of $E_{P,0}/\sqrt{2} = 7.3$ eV are indicated on the right.

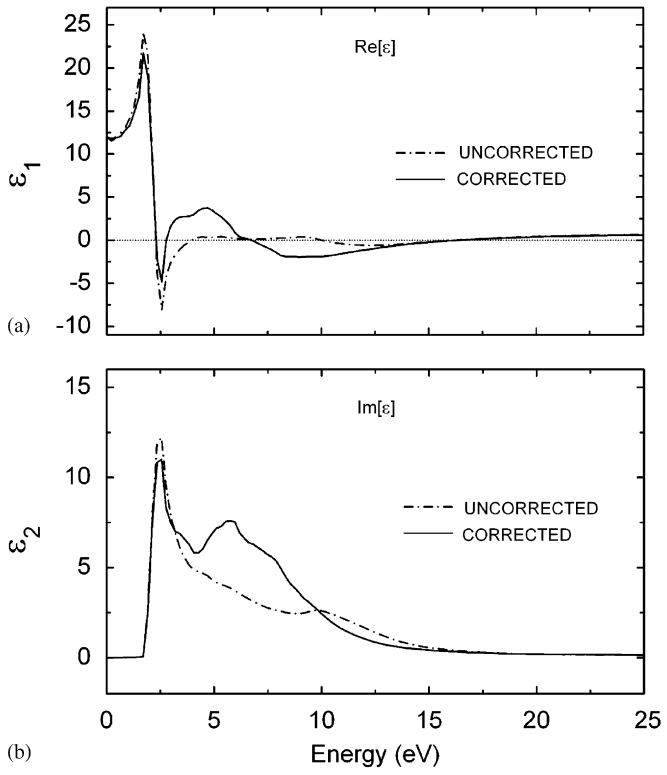

Fig. 11. The real and imaginary parts of the dielectric function of Si deduced from SSD. The curves labelled 'corrected' correspond to results when surface-losses were removed. The specimen thickness is 420 Å corresponding to SSD #2 in Figs. 4(b) and 5(b).

In Fig. 11 the resulting $Re\{\varepsilon\}$ and $Im\{\varepsilon\}$ are presented. Here, the analysis was applied to SSD #2 (420 Å). The dielectric functions were obtained with and without removal of surface losses (curves #2 in Figs. 4(b) and 5(b)). In the Kramers–Kronig analysis the value of $\varepsilon(0) = 12.0$ for Si was used [39] as a normalization constant to compensate the unknown proportionality coefficient in Eq. (15).

Improvements in the dielectric function with the removal of surface-losses are striking. Peaks in the 4–8 eV region of $Im\{\varepsilon(E)\}$, characteristic of interband transitions, are damped heavily in the 'uncorrected' spectra. For thicker samples the contributions from surface losses become smaller and, therefore, starting from some thickness the effects of surface losses can be neglected. Detailed analysis [30] suggests that removal of surface losses is crucial for thicknesses up to 800 Å (or $0.65\lambda_{PL}$) of Si.

Comparison with optical measurements [39] indicates that the features in the 0–4 eV region of the dielectric function obtained here are not sufficiently accurate. As was mentioned earlier problems with energy resolution and large channel size in the measured EELS spectra cause inaccuracies in this region during retrieval of the SSDs. The presence of 10 Å SiO_2 layers on both surfaces of the specimen also modifies the results intended for pure crystalline Si [40].

4. Conclusion

In conclusion, we introduce a new approach for the separation of bulk and surface losses in low-loss EELS spectra measured in STEM. The assumption is that the surface losses are independent of thickness above a particular thickness while the bulk losses vary linearly with thickness. Two low-loss EELS data measured at different thicknesses is sufficient for analysis. The limitations of the method are also discussed.

For silicon we obtained critical parameters characterizing the bulk plasmon excitation such as $E_{P,0}$, the damping parameter ΔE_P and the coefficient of dispersion relation γ. This was achieved with a new numerical curve fitting procedure allowing all parameters be determined simultaneously. The results are in good agreement with values reported in literature. A by-product of the analysis is a quantitative explanation of the shape of the angle-integrated plasmon energy loss.

The possibility of separating surface-losses from bulk-losses allowed quantitative study of the effects of oxide layer coating. The analysis indicate that a few minutes exposure to the air was sufficient to create a 10 Å SiO_2 layer on both surfaces of the specimen. Comparisons of the dielectric functions retrieved from EELS data with and without including surface-losses indicate that even for samples as thick as 800 Å the effects of surface excitation can be significant.

Acknowledgments

This work is supported primarily by the Nanoscale Science and Engineering Initiative of the NSF EEC-0117770 and NYSTAR C020071. The sample preparation facilities and STEM are supported by NSF through the CCMR DMR 9632275. We would also like to acknowledge M. Thomas for technical support.

Appendix A

A.1. Surface-loss cross-section

For the sample of the thickness t and with parallel surfaces the cross-section for non-radiative surface plasmon-loss in case of an isotropic material at oblique incidence where only p-polarized waves are considered is given as [31]

$$\frac{\partial^2\sigma_s}{\partial E\,\partial\Omega} = \frac{P_0^2}{\hbar^2}\frac{2e^2}{\pi^2\hbar^2v^2\cos(\alpha_t)}Im\left[\frac{(\varepsilon-\varepsilon_0)^2}{\Phi_0^4\Phi^4}\right.$$
$$\times\left\{\left(\frac{\sin^2(q_xt/2)}{L^+}+\frac{\cos^2(q_xt/2)}{L^-}\right)\frac{B^2}{\varepsilon\varepsilon_0}\right.$$
$$-\left(\frac{\cos^2(q_xt/2)\tanh(\chi t/2)}{L^+}\right.$$

$$+\frac{\sin^2(q_x t/2)\coth(\chi t/2)}{L^-}\Big)A^2\chi\chi_0 + \left(\frac{1}{L^+}-\frac{1}{L^-}\right)\frac{\chi_0}{\varepsilon_0}AB\sin(q_x t)\Bigg\}\Bigg], \quad (A.1)$$

where P_0 and v are the momentum and velocity of the incident electron, α_t is the angle of incidence relative to specimen surface normal, ε and ε_0 are dielectric functions of the specimen and of the surrounding, $\beta = v/c$ (for 100 keV electrons $\beta^2 \cong 0.3$),

$$\chi_0 = (q_s^2 - \varepsilon_0\omega^2/c^2)^{1/2}, \quad (A.2)$$

$$\chi = (q_s^2 - \varepsilon\omega^2/c^2)^{1/2}, \quad (A.3)$$

$$\Phi_0^2 = q^2 - \varepsilon_0\omega^2/c^2, \quad (A.4)$$

$$\Phi^2 = q^2 - \varepsilon\omega^2/c^2, \quad (A.5)$$

$$\Phi_1^2 = \Phi^2 - \varepsilon_0\omega^2/c^2, \quad (A.6)$$

$$L^+ = \chi_0\varepsilon + \chi\varepsilon_0\tanh(\chi t/2), \quad (A.7)$$

$$L^- = \chi_0\varepsilon + \chi\varepsilon_0\coth(\chi t/2), \quad (A.8)$$

$$B = q_s\Phi_1^2 + \varepsilon\varepsilon_0\beta^4[\omega/v]^3\sin(\alpha_t)\cos(\phi), \quad (A.9)$$

$$A = [q_s - q_x\tan(\alpha_t)\cos(\phi)][\omega/v]\beta^2\cos(\alpha_t) \quad (A.10)$$

and α_t is specimen tilt angle relative to normal incidence (see Fig. A.1). Here q_s is the component of the scattering vector parallel to the specimen surface which can be expressed as

$$q_s = k_0\theta\cos(\alpha_t\cos(\phi))\left[1+\frac{\theta_E}{\theta}\tan(\alpha_t\cos(\phi))\right]. \quad (A.11)$$

Here, $\alpha_t\cos(\phi)$ is the angle between q_s and surface normal to $\vec{k}_0$. In the derivation of expression (A.1) the coordinate axes were chosen such that the x-axis is along the line perpendicular to the surface and $q_s(0, q_y, q_z)$. The dependence of the cross-section on scattering angle and energy-loss closely follows that of surface plasmon dispersion. Two dispersion equations describing surface plasmon excitations can be obtained by taking $L^+ = 0$ and $L^- = 0$.

The expression (A.1) can be greatly simplified if we take into account that: (i) the terms containing β^4 can be dropped since their contributions are small and (ii) since the thicknesses of the specimens are >30 nm, $qt \gg 1$ and,

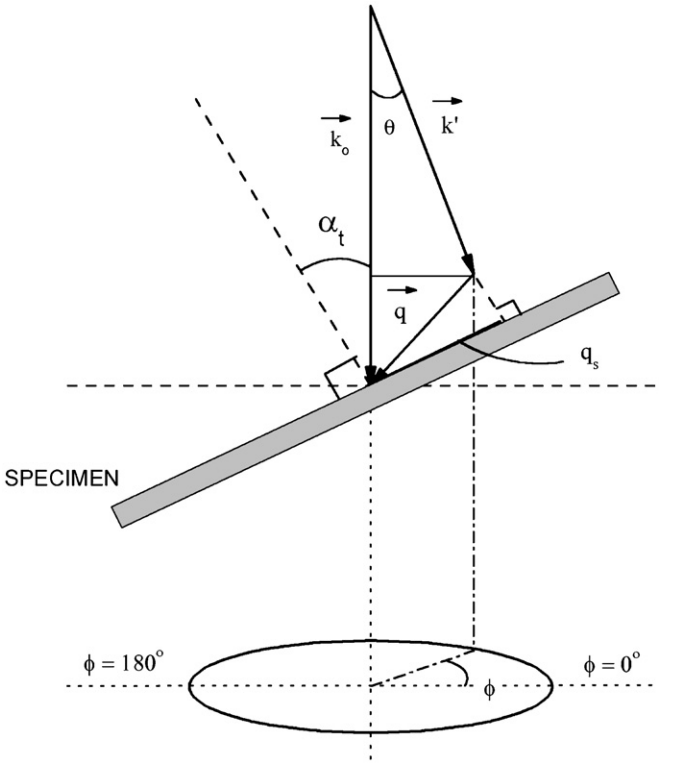

Fig. A.1. Simple diagram of incident and scattered electrons creating surface plasmon excitations. The azimuthal angle ϕ is in the plane perpendicular to the incident wave vector $\vec{k}_0$.

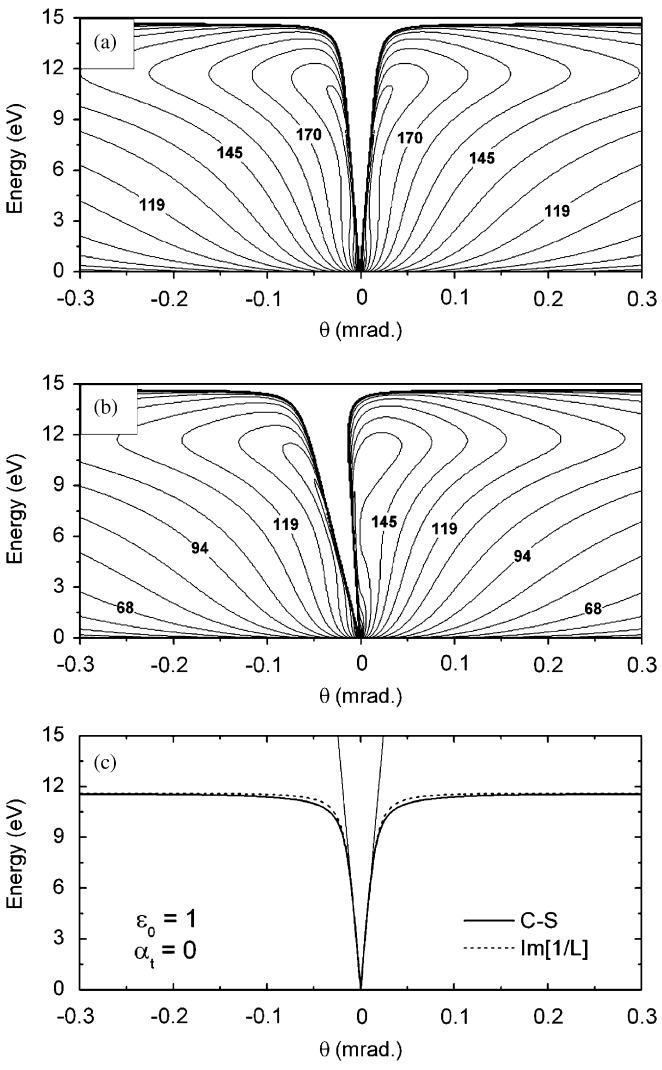

Fig. A.2. Calculated cross-section of non-radiative surface plasmon excitations caused by 100 keV electrons in a typical Si sample. The graphs are in logarithmic scale. The following values were used in Eq. (A.12) for this simulation: $\varepsilon_0 = 1$, $E_{P,0} = 16.6$ eV and $\Delta E_P = 3.5$ eV. In (a) $\alpha_t = 0$ and in (b) $\alpha_t = 30°$, $\phi = 0°$. (c) The lines of maximum intensities calculated for cross-section (C-S) presented in (a) and for a function $Im\{1/L\}$.

therefore, $\tanh(\chi t/2) \cong \coth(\chi t/2) \cong 1$. The expression for the cross-section (A.1) now can be rewritten as

$$\frac{\partial^2\sigma_s}{\partial E\,\partial\Omega} = \frac{2e^2P_0^2}{\pi^2\hbar^4v^2\cos(\alpha_t)}\,Im\left\{\frac{(\varepsilon-\varepsilon_0)^2}{\varepsilon\varepsilon_0 L}\,\frac{q_s^2\Phi_1^4}{\Phi_0^4\Phi^4}\right\}, \tag{A.12}$$

where no splitting of the dispersion curves is expected and

$$L \equiv L^+ = L^- \cong \chi_0\varepsilon + \chi\varepsilon_0. \tag{A.13}$$

In Figs. A.2(a) and (b) the contour-plots of the cross-sections that were calculated using expression (A.12) for non-radiative surface plasmons are presented. At high scattering angles the dispersion curves as well as cross-sections approach limiting values of $E = E_{P,0}/\sqrt{2}$. Asymmetry caused by non-normal incidence is apparent in Fig. A.2(b). It should be noted that the cross-section is symmetric at $\phi = 90^\circ$ for any tilt angle.

As was noted earlier, the behavior of the cross-section follows closely the behavior of the dispersion curves. This can be best illustrated by comparing the lines of maximum value of the cross-section (A.12) and function $Im\{1/L\}$. The maxima of the function $Im\{1/L\}$ are at the dispersion lines where $L = 0$. Both the cross-section and the function $Im\{1/L\}$ are continuous, well-behaving functions with single, well-defined peaks. Fig. A.2(c) shows that the differences between them are very small. The calculations in Fig. A.2(c) for lines of maximum intensity of the cross-section were done with the same parameters as in Fig. A.2(a), and therefore direct comparison can be made.

References

[1] P.E. Batson, O.L. Krivanek, N. Dellby, Nature 418 (2002) 617.
[2] P.M. Voyles, D.A. Muller, J.L. Grazul, P.H. Citrin, H.-J.L. Gossmann, Nature 416 (2002) 826.
[3] P.E. Batson, K.L. Kavanagh, J.M. Woodall, J.W. Mayer, Phys. Rev. Lett. 57 (1986) 2729.
[4] J. Bruley, P.E. Batson, Phys. Rev. B 40 (1989) 9888.
[5] M. Varela, S.D. Findlay, A.R. Lupini, A.Y. Borisevich, N. Dellby, O.L. Krivanek, P.D. Nellist, M.P. Oxley, L.J. Allen, S.J. Pennycook, Phys. Rev. Lett. 92 (2004) 095502.
[6] H. Watanabe, J. Phys. Soc. J. 11 (1956) 112.
[7] H. Raether, in: G. Höhler (Ed.), Springer Tracts in Modern Physics, vol. 38, Springer, Berlin, 1965, p. 85.
[8] P.E. Batson, J. Silcox, Phys. Rev. B 27 (1983) 5224.
[9] R.F. Egerton, Electron Energy Loss Spectroscopy in the Electron Microscope, second ed., Plenum Press, New York, 1996.
[10] R. Vincent, J. Silcox, Phys. Rev. Lett. 31 (1973) 1487.
[11] R.B. Pettit, J. Silcox, R. Vincent, Phys. Rev. B 11 (1975) 3116.
[12] C.H. Chen, J. Silcox, R. Vincent, Phys. Rev. B 12 (1975) 64.
[13] R.D. Leapman, P.L. Fejes, J. Silcox, Phys. Rev. B 28 (1983) 2361.
[14] M. Isaacson, J. Chem. Phys. 56 (1972) 1803.
[15] N.D. Browning, J. Yuan, L.M. Brown, Ultramicroscopy 38 (1991) 291.
[16] K.A. Mkhoyan, Ph.D. Thesis, Cornell University, Ithaca, NY, 2004.
[17] J.M. Cowley, A.F. Moodie, Acta. Cryst. 10 (1957) 609.
[18] E.J. Kirkland, Advanced Computing in Electron Microscopy, Plenum Press, New York, 1998.
[19] D.W. Johnson, J.C.H. Spence, J. Phys. D 7 (1974) 771.
[20] P.A. Crozier, R.F. Egerton, Ultramicroscopy 27 (1989) 9.
[21] R.F. Egerton, Z.L. Wang, Ultramicroscopy 32 (1990) 137.
[22] P.E. Batson, Phys. Rev. Lett. 57 (1986) 2729.
[23] P.E. Batson, Ultramicroscopy 78 (1999) 33.
[24] H. Raether, in: G. Höhler (Ed.), Springer Tracts in Modern Physics, vol. 88, Springer, Berlin, 1980.
[25] R.F. Loane, P. Xu, J. Silcox, Acta. Cryst. A 47 (1991) 267.
[26] R.H. Ritchie, Phys. Rev. 106 (1957) 874.
[27] R.H. Ritchie, A. Howie, Philos. Mag. 36 (1977) 463.
[28] W.H. Press, S.A. Teukolsky, W.T. Vetterling, B.P. Flannery, Numerical Recipes in C++, Cambridge University Press, Cambridge, MA, 2002, p. 413.
[29] J.A. Nelder, R. Mead, Comput. J. 7 (1965) 308.
[30] K.A. Mkhoyan, T. Babinec, J. Silcox, unpublished.
[31] E. Kroger, Z. Physik 235 (1970) 403.
[32] E. Kroger, Z. Physik 216 (1968) 115.
[33] H. Raether, Phys. Thin Films 9 (1975) 273.
[34] C.H. Chen, J. Silcox, Solid State Commun. 17 (1975) 64.
[35] T. Kloos, Z. Physik 208 (1968) 77.
[36] S.M. Sze, Physics of Semiconductor Devices, second ed., Wiley, New York, 1981.
[37] J. Daniels, C.V. Festenberg, H. Raether, K. Zeppenfeld, in: G. Höhler (Ed.), Springer Tracts in Modern Physics, vol. 54, Springer, Berlin, 1970, p. 77.
[38] D.W. Johnson, J. Phys. A 8 (1975) 490.
[39] D.E. Aspnes, A.A. Studna, Phys. Rev. B 27 (1983) 985.
[40] K.A. Bell, L. Mantese, U. Rossow, D.E. Aspnes, Thin Solid Films 313–314 (1998) 161.